Contactless and absolute linear displacement detection based upon 3D printed magnets combined with passive radio-frequency identification

Roman Windl, Claas Abert, Florian Bruckner, Christian Huber, Christoph Vogler, Herbert Weitensfelder, and Dieter Suess

---

Articles you may be interested in

3D print of polymer bonded rare-earth magnets, and 3D magnetic field scanning with an end-user 3D printer
Applied Physics Letters **109**, 162401 (2016); 10.1063/1.4964856

Topology optimized and 3D printed polymer-bonded permanent magnets for a predefined external field
Journal of Applied Physics **122**, 053904 (2017); 10.1063/1.4997441

A fast finite-difference algorithm for topology optimization of permanent magnets
Journal of Applied Physics **122**, 113904 (2017); 10.1063/1.4998532

Noise reduction in heat-assisted magnetic recording of bit-patterned media by optimizing a high/low Tc bilayer structure
Journal of Applied Physics **122**, 213903 (2017); 10.1063/1.5004244

Effective uniaxial anisotropy in easy-plane materials through nanostructuring
Applied Physics Letters **111**, 192407 (2017); 10.1063/1.4997816

Passive wireless strain measurement based upon the Villari effect and giant magnetoresistance
Applied Physics Letters **109**, 253502 (2016); 10.1063/1.4972399

Contactless and absolute linear displacement detection based upon 3D printed magnets combined with passive radio-frequency identification

Roman Windl,[1,a] Claas Abert,[1] Florian Bruckner,[1] Christian Huber,[1] Christoph Vogler,[2] Herbert Weitensfelder,[1] and Dieter Suess[1]

[1]*CD-Laboratory: Advanced Magnetic Sensing and Materials, University of Vienna, Physics of Functional Materials, Währinger Straße 17, 1090 Vienna, Austria*
[2]*University of Vienna, Physics of Functional Materials, Währinger Straße 17, 1090 Vienna, Austria*

Within this work a passive and wireless magnetic sensor, to monitor linear displacements, is proposed. We exploit recent advances in 3D printing and fabricate a polymer bonded magnet with a spatially linear magnetic field component corresponding to the length of the magnet. Regulating the magnetic compound fraction during printing allows specific shaping of the magnetic field distribution. A giant magnetoresistance magnetic field sensor is combined with a radio-frequency identification tag in order to passively monitor the exerted magnetic field of the printed magnet. Due to the tailored magnetic field, a displacement of the magnet with respect to the sensor can be detected within the sub-mm regime. The sensor design provides good flexibility by controlling the 3D printing process according to application needs. Absolute displacement detection using low cost components and providing passive operation, long term stability, and longevity renders the proposed sensor system ideal for structural health monitoring applications. https://doi.org/10.1063/1.5004499

I. INTRODUCTION

Linear displacement systems in the mm regime are widely used among different industries. A huge variety of measuring techniques is currently available, for example infra-red, ultra-sonic, magnetic,[1–3] optic[4] or even digital picture processing. Applications which demand passive, wireless and long term operation, like for example structural health monitoring, are the main scope of the presented displacement detection approach. The proposed sensor setup consists of three main parts: (i) an radio-frequency identification (RFID) tag, (ii) a giant magnetoresistance (GMR) magnetic field sensor combined with an instrumentation amplifier (IAMP) and (iii) a 3D printed polymer bonded magnet, shown in FIG. 1. With a combination of (i), and (ii) it is possible to passively monitor different physical properties like temperature,[5] or strain.[6]

This work presents a displacement detection technique based on 3D printed magnets with a spatially linear magnetic field component, at a specific region along the stretched axis of the magnet. The approach of varying the magnetic compound fraction ρ_m by 3D printing polymer bonded magnetic materials allows magnetic field shaping as presented by Huber et al.[7–9] Additionally these publications contain detailed material, printing, and simulation descriptions. Designing the magnetic field magnitudes according to the characteristics of the used magnetic field sensor increases measurement resolution and enables new types of applications. The main advantages of the presented sensor method are the absolute displacement detection, passive operation, commercially available

---

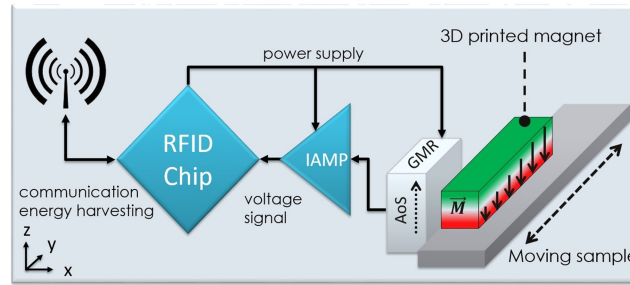[a]Electronic mail: roman.windl@univie.ac.at

FIG. 1. A schematic of the sensor system is illustrated. The magnetization of the 3D printed magnet points along negative z-axis. A GMR sensor with an axis of sensitivity (AoS) along positive z-axis observes the resulting spatially linear magnetic field change if the sample is moved along y-axis. The movement along other x-, and z-axis has to be prevented.

and low cost components, long term stability, longevity and low soil influence. Hence, hazardous, or very dusty environments are possible areas of application.

A 3D printer with a mixing extruder is used in order to fabricate a polymer bonded magnet with varying magnetic compound fraction. Since the magnetic field range of the GMR sensor is in the mT regime, a hard ferrite is a suitable permanent magnet, because the magnetic remanence B_r allows to induce magnetic flux densities high enough. As magnetic material a hard ferrite ($SrOx_6Fe_2O_3$) inside a PA6 matrix called Sprox® 10/20p from Magnetfabrik Bonn is used. Supplying the mixing extruder with a pure PA6 nylon and Sprox® 10/20p allows to regulate the magnetic compound fraction ρ_m from 0% to 100%. Parameters like the start compound fraction $\rho_{m,0}$, stop compound fraction ρ_{m,l_y} and magnetization are tuned to match a specific magnetic field magnitude at these points.

II. SIMULATIONS

In order to describe the advantages of 3D printing polymer bonded magnets, a the micromagnetic finite-element simulation code called magnum fe[10] is used. The linear displacement detection is based upon an uni-directional GMR sensor. Hence, a single magnetic field component is shaped to incorporate a spatial linear increase which correlates to a position of the permanent magnet. This behaviour can be achievable with multiple shapes, or magnetic compound fractions. Within this work only linear compound fractions and linear shapes are used, because it demonstrates the advantages of varying magnetic compound fractions for fast prototyping and simple shapes. 3D printing polymer bonded magnets of complex shapes allows to test them, before manufacturing an expensive mold. Most polymer bonded magnets are injection molded and afterwards magnetized inside a constant external magnetic field. The 3D printed part is incorporated by a cuboid shape with dimensions 10 mm × 40 mm × 10 mm ($l_x \times l_y \times l_z$). In order to simulate a linear increase of ρ_m from 0 % at $y = 0$ mm to 100% at $y = 40$ mm the magnetization is scaled in the same way. Resulting in $J_{z,min} = 0$ T at $y = 0$ mm increasing to $J_{z,max} = -0.45$T at $y = 40$ mm, see Fig. 2a. On the other hand, an injection molded part is represented by a pyramid shape with the apex at $x, y, z = 0$ mm the base at $y = 40$ mm and with a side length of $l_x, l_z = 10$ mm. The pyramid has a constant magnetization $J_z = -0.45$T, see Fig. 2b. The resulting magnetizations are visualized within Fig. 2.

The used J_s values are too high compared to the J_s of Sprox® 10/20, but they are suitable for demonstration purposes. These two shapes will result in similar spatially linear magnetic field distributions of B_z, rendering them ideal for comparison. Fig. 3 illustrates the planes used for magnetic field evaluation.

A field box around the magnetic shape, where the magnetic field gets calculated, is defined with a size of 20 mm × 60 mm × 20 mm. The magnetic shapes are centered in all directions within the field box. $y = 0$ mm represents the beginning of the magnetic shapes.

The magnetic field around the chosen shapes is evaluated at two sides, representing possible sensor planes, called A and B see Fig. 3 for illustration. d describes the distance between the magnetic shapes base and the plane. For plane A d is along the x-axis and d is along the z-axis for plane B.
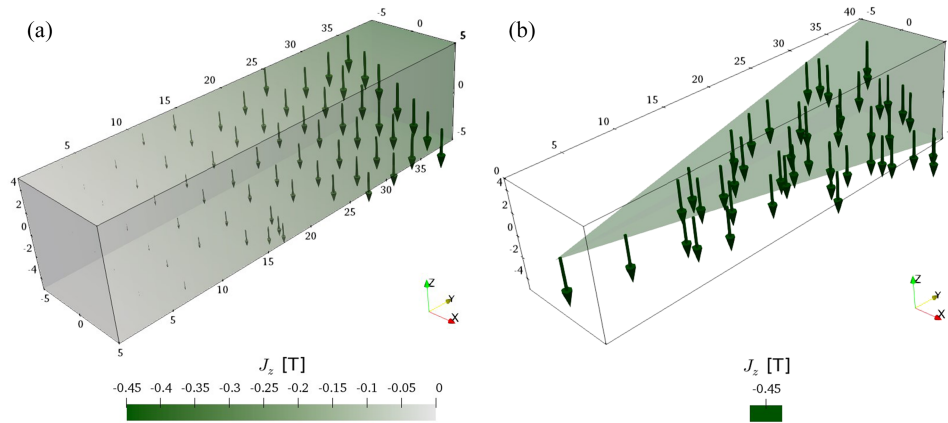
FIG. 2. (a) Cuboid shaped magnet with a linear increasing magnetization along the y-axis. (b) Constant magnetization of the pyramid shape is illustrated.
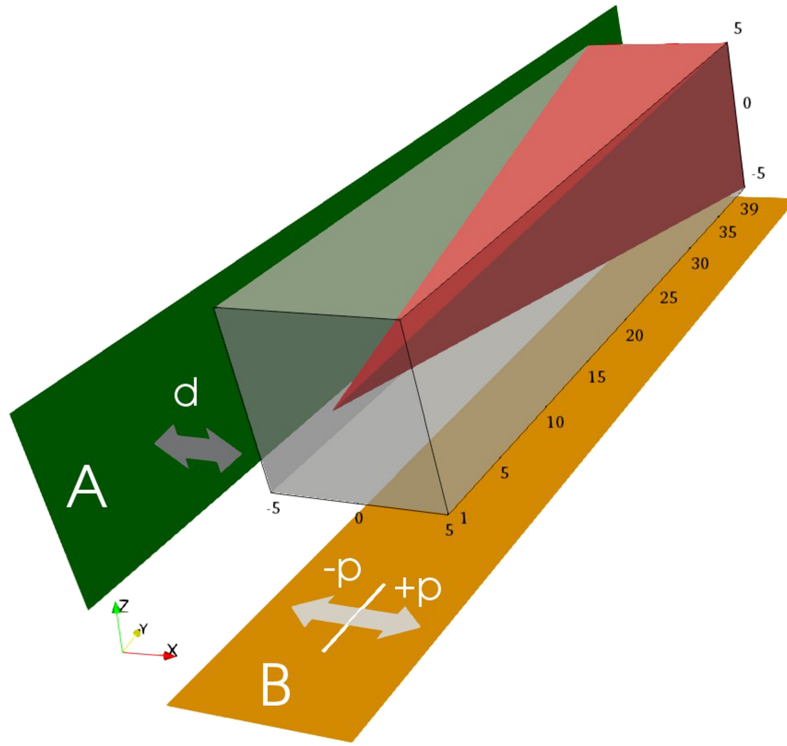

FIG. 3. Plane A as well as B are used to evaluate the magnetic field generated by the cuboid shape (grey) and the pyramid shape (red). The base of the pyramid is used to dimension d.

Additionally, p is used to describe the distance to the center along the planes width. Main comparison attributes are: (1) the linearity of B_z along y-axis for plane A, (2) p dependency of B_z, and (3) p dependency of B_x and B_y. First of all, B_z is plotted along the y-axis for plane A and B within Fig. 4 with different d values.

Increasing d, decreases the maximum abs(B_z) value and moves the y positions of this point slightly outwards, which respectively increases the linear region. This allows to adjust the linear region and the maximum B_z with d, in order to fit specific requirements. For example the linear range of the GMR sensor. It is clearly visible that plane B has a better linearity with longer y-axis elongation for the cuboid shape. Interestingly this is in contrast to the pyramid shape where plane A results in a
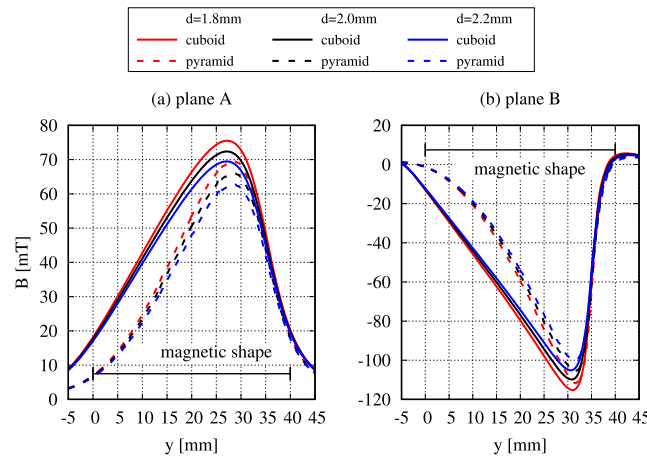
FIG. 4. (a) Indicates the B_z values for the cuboid shape with linear increasing magnetization and a pyramid shape with constant magnetization along path A. On the other hand (b) represents B_z for path B. A difference in linearity and maximum B_z value between pyramid and cuboid shape is noticed.
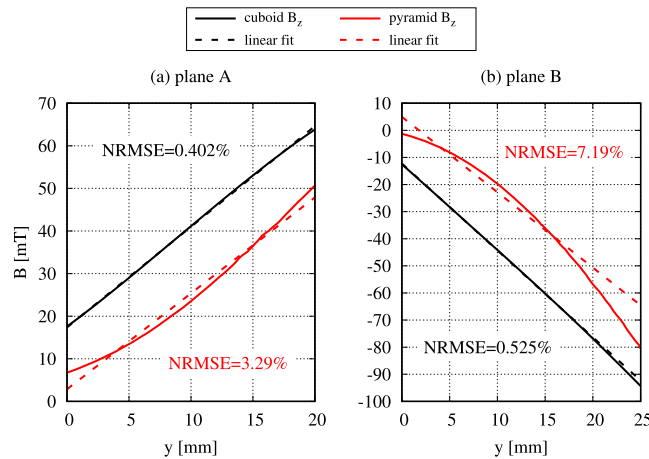

FIG. 5. Fitting the linear regions of both magnetic shapes indicates large errors for the pyramid shape. The normalized root mean square error (NRMSE) is noted in order to describe the linearity error.

more exact linear dependence. But for both planes the cuboid shape, with magnetization variation, results in better linearity with higher B_z values. Fig. 5 illustrates the linearity error for B_z values fitted with a linear transfer function at $d = 2.0$ mm.

At plane A the pyramid shape with constant magnetization has an about 8 times higher normalized root mean square error (NRMSE) compared to the cuboid shape with linear magnetization. On the other hand, for plane B, the NRMSE of the pyramid is about 13.5 times higher. These significant differences highlight a better linear performance of the cuboid shape.

III. 3D PRINTED MAGNET

The magnetic compound fraction is varied from $\rho_{m,0} = 10\%$, resulting in composition of 10% Sprox® 10/20p and 90% PA6, to $\rho_{m,\text{ly}} = 80\%$ in order to match the linear range of the used GMR sensor. The magnet is printed along y-axis with a layer heigh of 0.15 mm, leading to $\Delta\rho_m \approx 0.26\%$ for each layer. Due to printing irregularities the true size of the magnet, after the printing process, is 9.5 mm $\times$ 39 mm $\times$ 9.5 mm ($l_x \times l_y \times l_z$) instead of 10 mm $\times$ 40 mm $\times$ 10 mm ($l_x \times l_y \times l_z$). An
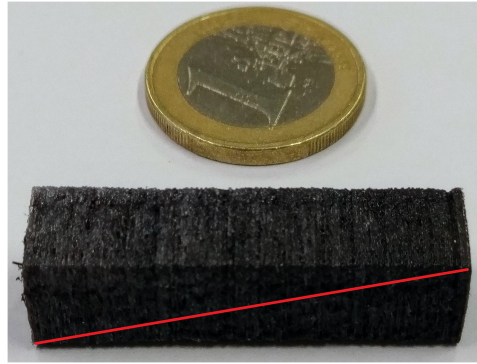
FIG. 6. Picture of the 3D printed magnet with a size of 9.5 mm × 39 mm × 9.5 mm. The red line represents the increasing magnetic compound fraction.

electromagnet is used to magnetize the 3D printed cuboid with $B_z = -0.3$T. y describes the position along the y-axis of the magnet. Fig. 6 illustrates a picture of the 3D printed magnet.

IV. 3D MAGNETIC FIELD SCANNING

Huber et al.[7] also showed how to upgrade the 3D printer with a TLV493D 3D magnetic field sensor from Infineon Technologies to perform a 3D scan of the magnetic field produced by an arbitrary sample. The same method is used to characterize the linearity of the magnetic field induced by the magnetization of the 3D printed magnet and is illustrated in FIG. 7.

Positioning the GMR sensor is very crucial in order to measure the spatially linear magnetic field component B_z. GMR sensors are in plane sensitive and placing the sensor at position A, see inset Fig. 7, allows larger distances between the permanent magnet and the sensor. Additionally, this position is more suitable due to the significantly smoother B_z component and smaller influences of the B_x and B_y components. The solid red line represents $-B_z$ at position B above the magnet from $y =$ 5 mm to $y = 33$ mm where a nearly linear increase is measurable. A noticeable deviation of linearity is recognized from $y = 15$ mm to $y = 28$ mm as a result of printing irregularities. However, at position A, sideways along the magnet, the B_z component represented by a solid blue line matches the GMR sensors linear range characteristics from $y = 0$ mm with $B_z = 0.5$ mT to $y = 26$ mm with $B_z = 3.5$ mT.
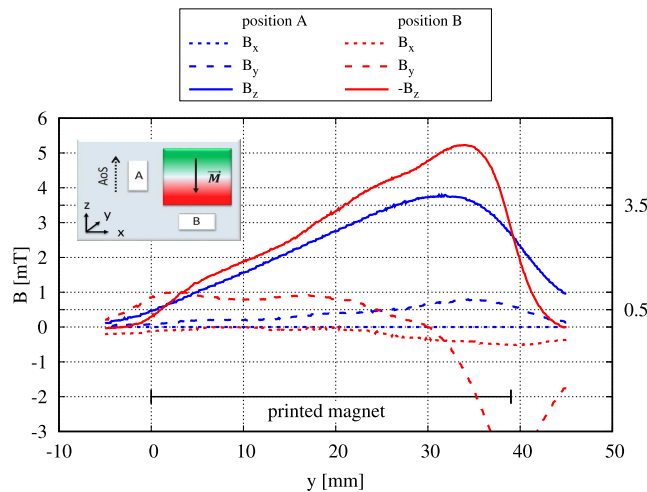

FIG. 7. The magnetic field is measured along the y-axis with a 3D hall probe at a distance of 2.2 mm. Because of printing irregularities the $-B_z$ component at position B (solid red line) does not increase perfectly linear.

V. RFID SYSTEM SETUP

Within the following paragraphs a detailed description of the single sensor components is provided. As RFID tag the SL900A[11] from AMS AG is used. The external sensor front-end (SFE) allows different voltage adjustments and ranges to offer a large variety of applications for the two analog inputs.

Because of the RFID tags analog to digital conversion with 10 bit the maximum value is $AD_{max} = 2^{10} = 1024$. Energy harvested by the reader field is converted in order to supply external sensors by the output supply voltage U_{EXC}. Because of the low current supplied $I_{EXC} < 200\,\mu A$ most Hall sensors are not applicable. Hence, GMR sensors with resistances $R > 15\,k\Omega$ are used to keep the power consumption as low as possible. Furthermore, GMR sensor introduce the advantage of long term stability without drift over time. As a magnetic field sensor the GMR AA006 from NVE Corporation with the following characteristics is used: $R_{GMR} = 30\,k\Omega \pm 20\%$, a linear range from 0.5 mT $< B_{ext} <$ 3.5 mT and saturation at $B_{sat} \approx 5$ mT. A downside of the used GMR sensor is a hysteresis of approximately 4% at unipolar operation and a temperature coefficient of voltage TCOV=−0.1% $°C^{-1}$. Because the RFID tag has an internal temperature sensor, incorporating temperature variations is possible, neglecting measurement error due to temperature changes. Due to the fact that GMR sensors are configured in a Wheatstone bridge setup two signal inputs are required. The measurable voltage difference is too small for the SFE characteristics and therefore an instrumentation amplifier helps to overcome this issue. The INA333 from Texas Instruments is an appropriate choice because of the low power consumption and the wide supply voltage. An additional advantage of using an instrumentation amplifier is that the GMR sensors output voltage can be adjusted to nearly match the specific analog input characteristics of the RFID tag. Supplying the RFID tag and other sensor components through the reader field decreases the reading distance due to the increased power consumption, as shown in Fig. 8. As an RFID reading device the Astra-EX from ThingMagic is used. If the distance to the reader is increased, a decreasing output supply voltage U_{EXC} of the RFID tag is monitored. Therefore, the GMR sensor is supplied by the U_{VRef} voltage, instead of the distance dependent EXC pin voltage U_{EXC}. Additionally, reducing the power consumption due to the lower GMR sensors supply voltage U_{VRef}. When the EXC pin voltage reaches 1.8V the AD uncertainty increases and the mean is decreased. After U_{EXC} drops below the minimum IAMP supply voltage of 1.8V, communication with the RFID tag is nearly impossible. The IAMP, approximately consumes 50 μA and the GMR sensor adds 10 μA which is below the defined $I_{EXC} < 200\,\mu A$. Keeping the power consumption as low as possible is crucial to allow passive operation. Therefore,
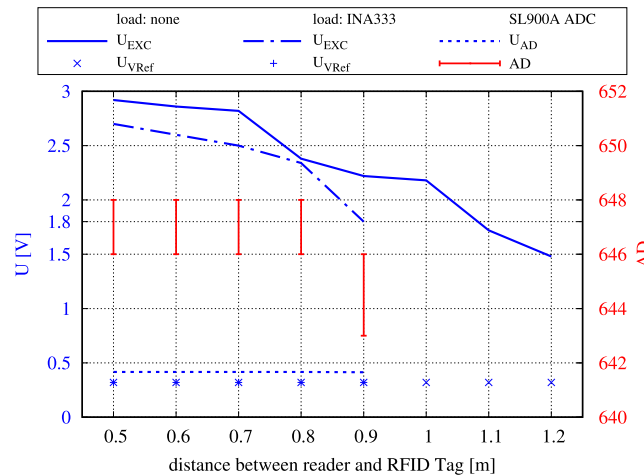

FIG. 8. Output voltage of the EXC pin U_{EXC} (solid and long dashed blue line) over the distance between the Astra-EX reader antenna and the SL900A. The V_{REV} pin voltage U_{VRef} (triangle up and triangle down in blue color) is stable until no communication is possible at all. Blue color indicates voltages and the red bars indicate the AD range. The IAMP output voltage (blue short dashed line) is steady over the whole voltage supply range.

perfectly adjusting the GMR sensors output voltage by further electronic components is not considered.

In order to measure the real magnetic field dependence and resolution the presented sensor system is calibrated inside a Helmholtz Coil. The distance between the RFID reader Astra-EX and the SL900A tag is 0.5m for all following measurements.

VI. LINEAR DISPLACEMENT CHARACTERISTICS

The external magnetic field B_{ext} is altered from 6 mT to 0 mT and backwards with 0.1 mT steps. Fig. 9 shows the measurement results and reveals hysteric behaviour.

The performed measurements at room temperature indicate a maximum measured magnetic field $B_{ext,max} = 5.4$ mT for the maximum analog to digital value $AD_{max} = 1023$. If the transfer function from Fig. 9 is fitted by a polynomial equation T_B, recalculation of the external applied magnetic field

$$B_{ext} = T_B(AD) \qquad (1)$$

is possible. In order to estimate the correlation between the y-axis position y_{pos} of the 3D printed magnet and the magnetic field value B at this position, a second transfer function T_M is introduced

$$y_{pos} = T_M(B) = \frac{\Delta l}{\Delta B_l} B. \qquad (2)$$

By combining equation 1, and 2, the conversion of AD into a y-axis position

$$y_{pos} = T_M(T_B(AD)) \qquad (3)$$

is achieved, allowing the recalculation of the magnets y-axis displacement with respect to the sensor position.

The distance between the GMR sensor as well as the permanent magnet regulates the maximum magnetic field and therefore is used to fit the GMR sensor range. Because the sensor calibration showed linearity up to 5.4mT the distance d between the GMR sensor and the permanent magnet is decreased to 1.8 mm, in order to utilize the whole linear range of the GMR sensor. With the GMR sensor mounted upon the 3D printers head, magnetic field measurements along the y-axis of the magnet are performed. By using the transfer function T_B from equation 1, recalculation of the external magnetic field B_{ext} is performed and illustrated in Fig. 10.

The AD resolution is given by

$$\sigma_{res} = \frac{1}{AD_{max}} = 0.097\,\%. \qquad (4)$$
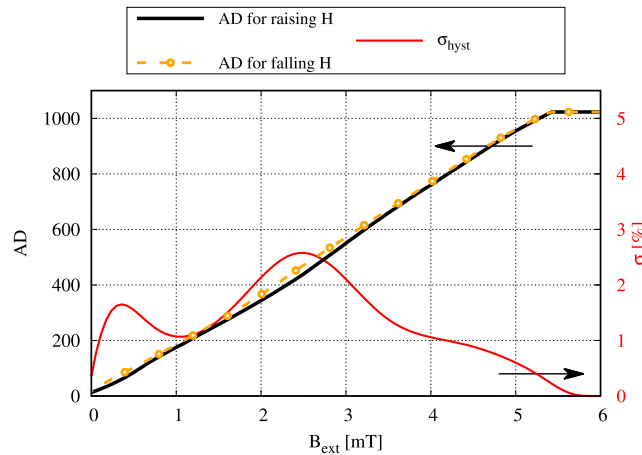

FIG. 9. The transfer function for the proposed sensor setup is shown. For raising H (black solid line, left axis) and falling H (orange dashed pointed line, left axis) a hysteresis induced measurement error δ_{hyst} (solid red line, right axis) is measured.
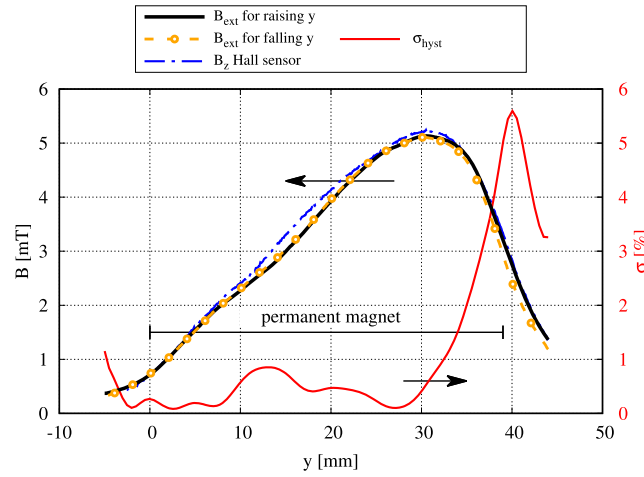
FIG. 10. B_z for the Hall Sensor TLV493D (blue dashed line, left axis) is compared to the recalculated B_{ext} for raising y from −5 mm to 44 mm (black solid line, left axis) and falling y from 44 mm to −5 mm (orange dashed pointed line, left axis). δ_{hyst} (red solid line, right axis) illustrates the hysteric influence.

ΔAD_{total} consists of all possible noise sources noted by

$$\Delta AD^2_{total} = \Delta AD^2_{ADC} + \Delta AD^2_{IAMP} + \Delta AD^2_{GMR} + \Delta AD^2_{ext} \qquad (5)$$

where the sources are represented by ΔAD_{ADC} the analog to digital converter noise, ΔAD_{IAMP} the noise from the IAMP, the GMR sensor noise ΔAD_{GMR} and external noise ΔAD_{ext}. A detectivity of $\approx 10\,\mathrm{n\,T}\sqrt{\mathrm{Hz}^{-1}}$ at $f = 0.1$ Hz was measured by Stutzke et al.[12] for the AA002 which has an approximately three times higher mean sensitivity than the AA006 rendering Δ_{GMR} negligible. The noise produced by the instrumentation amplifier, $\approx 3\,\mu V$ for DC operation with Gain $G_{IAMP} = 1$, is insignificant because it is clearly smaller than the analog to digital resolution. Hence, only ΔAD_{ADC} and ΔAD_{ext} are the main noise sources for the proposed measurement setup. For each measurement step hundred AD measurements are averaged, deviating by a noise induced minimum measurement error

$$\sigma_{noise} = \sqrt{\frac{\Delta AD^2_{tot}}{AD^2_{max}}} = 0.293\,\%. \qquad (6)$$

Fig. 10 indicates nearly linear behaviour in region l from $l_{min} = 0$ to $l_{max} = 30$ mm. Therefore, l is used as displacement detection region. Within this region the hysteresis induced measurement error

$$\sigma_{hyst} = \frac{AD_{hyst}}{AD_{max}} = 0.966\,\% \qquad (7)$$

is computed. The sensor characteristic properties are set in relation to displacement detection region l within TABLE I. The impact of deviations along x- and z-axis is also important for the sensors overall performance, see Fig. 3 for description. It is crucial to fix the movement of the printed magnet for the x- and z-axis. But the behaviour is measured and documented for better sensor description. Changes along the x-axis correlate to a change of distance between the printed magnet and the GMR

TABLE I. Calculation of length relations for $l_{min} = 0$ and $l_{max} = 30$ mm.

type	σ [%]	Δl [μm]
res	0.097	29.1
noise	0.293	87.9
hyst	0.966	289.8

system. Because $d = 1.8$ mm is used to define the sensor characteristics, the x-axis measurements are divided in the following steps 1.6 mm, 1.8 mm, 2.0 mm, and 2.2 mm, Δx values of -0.2 mm, 0.2 mm, and 0.4 mm are possible. The displacement error σ_x is calculated in respect to the highest sensing value $B_{ext,max} = 5.4$ mm by

$$\sigma_x = \frac{B_{0\,mm} - B_{\Delta d}}{B_{z,ext,max}} \tag{8}$$

for each Δd value. Fig. 11 illustrates the y-axis dependency of Δd displacements for the GMR system.

These deviations show symmetric behaviour, with negligible noise. Only the spatially linear region l from $y = 0$ to $y = 30$ mm is important for sensor operation. The z-axis displacement p behaviour, shown in Fig. 12, is represented by σ_z and $\sigma_{z,noise}$. Only $d = 1.8$ mm is illustrated for the GMR system, because it represents the relevant prototype x-axis value.

The minimum z-axis errors is at $y \approx 32$ mm, which represents the position of the maximum x-axis error. It is possible to store data within the RFID tag, this allows to modify the endpoints defining the relation between B and displacement. If a linear displacement detection device is mounted at the
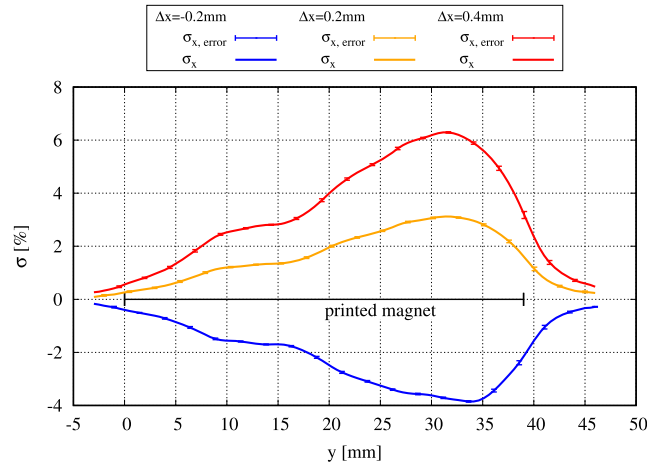

FIG. 11. The GMR systems displacement error σ_x and displacement noise $\sigma_{x,noise}$ along x-axis. σ_x increases until $y \approx 32$ mm.
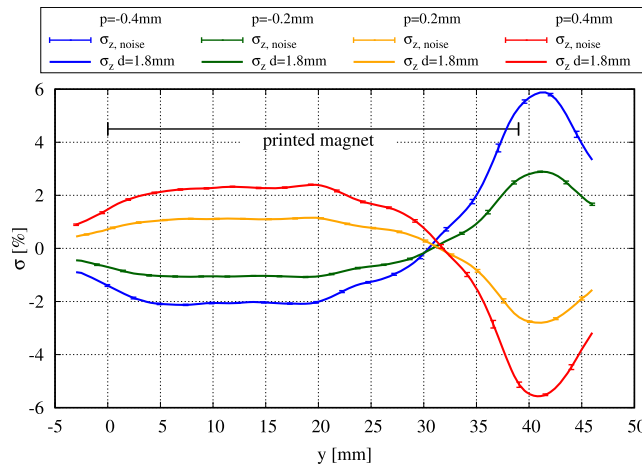

FIG. 12. Illustration of σ_z, along z-axis, with $d = 1.8$ mm and multiple p displacements. $\sigma_{x,min}$ is at $y \approx 32$ mm contrary to Fig. 11.

desired location, a test run can be initiated, in order to determine if the measured B is inside specified ranges and store them to increase accuracy.

Therefore, the detection of displacements within the sub-mm regime is possible. The magnet can be tuned towards application needs, for example it can be elongated or shortened to achieve predefined length resolutions with the advantage of absolute positioning. Additionally, the magnetic field can be shaped in order to reduce or even compensate the non linearity of the used GMR sensor by a specific compound fraction ρ_m variation. Hence, disadvantages of magnetic field sensor can be incorporated by system design, reducing post calculation complexity and therefore increasing the systems reliability. A hysteresis free GMR magnetic field sensor $\sigma_{\text{hyst}} = 0$ as presented by Brueckl et al.[13] and described by a patent[14] significantly decreases the detectable displacements.

VII. CONCLUSION AND OUTLOOK

The proposed displacement detection system consists out of three main components: (i) an RFID tag, (ii) a GMR magnetic field sensor combined with an IAMP, and (iii) a 3D printed polymer bonded magnet with linear magnetic compound fraction variation along the y-axis. The digital value AD of the analog to digital input of the RFID tag correlates to the magnets B_z component at a specific y-axis position. Main characteristics of the presented system are a resolution σ_{res} of 0.097%, a measurement uncertainty σ_{noise} of 0.293% and a hysteresis induced measurement uncertainty σ_{hyst} of 0.966%. Deviations along the other axis introduce detection errors. Therefore, the movement of along these axis must be prevented. Due to the fact of the possibility to store data upon the RFID tag, it is possible to set the start, middle, and end point when the sensor is mounted upon the target surfaces. Ensuring proper operation even if small deviations occur. Hence, displacements within sub-mm regime are detectable. The magnet can be tuned towards magnetic sensor characteristics[8,9] in order to utilize the whole linear range. Additionally, further adjustments of the magnet towards application needs are possible, for example decreasing or increasing the length of the overall position detection. Simulations are used to demonstrate the differences between, a simple linear magnetic compound fraction variation and a linear shape. The linearity of the magnetic field induced by the linear magnetic compound fraction has a higher accuracy, compared to a constant magnetized shape. This renders 3D printing polymer bonded magnets superior for fast prototyping and simple shapes. The precision of the presented system can be improved by replacing the used GMR sensor by a hysteresis free GMR sensor,[13,14] rendering $\sigma_{\text{hyst}} = 0$. The sensor design provides good flexibility adjusting to application needs by controlling the 3D printing process. Structural health monitoring is the main scope of application for the proposed passive, low cost, long term stable, and absolute displacement detection system.

ACKNOWLEDGMENTS

[1] C. Blache and G. Lamarquand, IEEE Transactions on Magnetics **28**, 2196 (1992).

[2] M. M. Miller, G. A. Prinz, P. Lubitz, L. Hoines, J. J. Krebs, S. F. Cheng, and F. G. Parsons, Journal of Applied Physics **81**, 4284 (1997).

[3] C. Roumenin and S. Lozanova, Sensors and Actuators A: Physical **138**, 37 (2007).

[4] W. B. Spillman, D. R. Patriquin, and D. H. Crowne, Appl. Opt. **28**, 3550 (1989).

[5] R. Windl, F. Bruckner, C. Abert, D. Suess, T. Huber, C. Vogler, and A. Satz, Journal of Applied Physics **117**, 17C125 (2015).

[6] R. Windl, F. Bruckner, C. Abert, C. Huber, C. Vogler, T. Huber, H. Oezelt, and D. Suess, Applied Physics Letters **109**, 253502 (2016).

[7] C. Huber, C. Abert, F. Bruckner, M. Groenefeld, O. Muthsam, S. Schuschnigg, K. Sirak, R. Thanhoffer, I. Teliban, C. Vogler, R. Windl, and D. Suess, Applied Physics Letters **109**, 162401 (2016).

[8] C. Huber, F. Bruckner, G. Martin, S. Stephan, T. Iulian, C. Vogler, G. Wautischer, W. Roman, and D. Suess, Scientific Reports **7** (2017).

[9] C. Huber, C. Abert, F. Bruckner, C. Pfaff, J. Kriwet, M. Groenefeld, I. Teliban, C. Vogler, and D. Suess, Journal of Applied Physics **122**, 053904 (2017).

[10] C. Abert, L. Exl, F. Bruckner, A. Drews, and D. Suess, Journal of Magnetism and Magnetic Materials **345**, 29 (2013).

[11] N. S. Saini, R. J. Burkholder, and J. L. Volakis, in *2016 IEEE International Symposium on Antennas and Propagation (APSURSI)* (2016) pp. 1277–1278.

[12] N. A. Stutzke, S. E. Russek, D. P. Pappas, and M. Tondra, Journal of Applied Physics **97** (2005).

[13] H. Brueckl, A. Satz, K. Pruegl, T. Wurft, S. Luber, W. Raberg, J. Zimmer, and D. Suess (2017) pp. 1–1.

[14] J. Zimmer, A. Satz, W. Raberg, H. Brueckl, and D. Suess, "Device, magnetic sensor device and method" (2015).